

# Reconstruction-Free Quantum Sensing of Arbitrary Waveforms

**Journal Article****Author(s):**

Zopes, Jonathan; Degen, Christian L.

**Publication date:**

2019-11

**Permanent link:**

<https://doi.org/10.3929/ethz-b-000380018>

**Rights / license:**

[In Copyright - Non-Commercial Use Permitted](#)

**Originally published in:**

Physical Review Applied 12(5), <https://doi.org/10.1103/PhysRevApplied.12.054028>

**Funding acknowledgement:**


175600 - Nanoscale magnetic imaging with diamond quantum sensors (SNF)

820394 - Advancing Science and TEchnology thRough dIamond Quantum Sensing (EC)

# Reconstruction-Free Quantum Sensing of Arbitrary Waveforms

J. Zopes\* and C.L. Degen†

*Department of Physics, ETH Zurich, Otto Stern Weg 1, 8093 Zurich, Switzerland*

 (Received 21 June 2019; revised manuscript received 20 September 2019; published 12 November 2019)

We present a protocol for directly detecting time-dependent magnetic field waveforms with a quantum two-level system. Our method is based on a differential refocusing of segments of the waveform using spin echoes. The sequence can be repeated to increase the sensitivity to small signals. The frequency bandwidth is intrinsically limited by the duration of the refocusing pulses. We demonstrate detection of arbitrary waveforms with approximately 20 ns time resolution and approximately  $4 \mu\text{T}/\sqrt{\text{Hz}}$  field sensitivity using the electronic spin of a single nitrogen-vacancy center in diamond.

DOI: [10.1103/PhysRevApplied.12.054028](https://doi.org/10.1103/PhysRevApplied.12.054028)

## I. INTRODUCTION

Well-controlled two-level quantum systems with long coherence times have proven useful for precision sensing [1,2] of various physical quantities including temperature [3], pressure [4], and electric [5] and magnetic [6,7] fields. By devising suitable coherent control sequences, such as dynamical decoupling [8], quantum sensing has been extended to time-varying signals. In particular, coherent control schemes have allowed the recording of frequency spectra [9–11] and lock-in measurements of harmonic test signals [12].

A more general task is the recording of arbitrary waveform signals, as an analogy to the oscilloscope in electronic testing and measurement. In this case, conventional dynamical decoupling sequences are no longer the method of choice, as the sensor output is nontrivially connected to the input waveform signal, requiring alternative sensing approaches. For slowly varying signals, the transition frequency of the sensor can be tracked in real time [13], permitting detection of arbitrary waveforms in a single shot. By using a large ensemble of quantum sensors, detection bandwidths of up to approximately 1 MHz have been demonstrated [14,15], with applications in MRI-tomograph stabilization [14], neural signaling [16,17], and magnetoencephalography [18].

For rapidly changing signals, the waveform can no longer be tracked and a general waveform cannot be recorded in a single shot. However, if a waveform is repetitive or retriggerable, multiple passages of the waveform can be combined to reconstruct the full waveform signal. This method, known as equivalent-time sampling, is routinely implemented in digital oscilloscopes to capture signals at effective sampling rates that are much higher

than the rate of analog-to-digital conversion. In quantum sensing, one possibility is to record a series of time-resolved spectra that cover the duration of the waveform [19]. This method, however, is limited to strong signals because the spectral resolution scales inversely with the time resolution. Other approaches include pulsed Ramsey detection [20], Walsh dynamical decoupling [21,22], and Haar wavelet sampling [23], discussed below. These methods use coherent control of the sensor to achieve competitive sensitivities but require some form of waveform reconstruction.

In this work, we experimentally demonstrate a simple quantum sensing sequence for directly recording time-dependent magnetic fields, with no need for signal reconstruction. Our method uses a spin echo to differentially detect short segments of the waveform and achieves simultaneous high magnetic field sensitivity and high time resolution. The only constraints are that the waveform can be triggered twice within the coherence time of the sensor and that the signal amplitude remains within the excitation bandwidth of qubit control pulses. Possible applications include the *in situ* calibration of miniature radio-frequency transmitters [19,24], activity mapping in integrated circuits [25], detection of pulsed photocurrents [26], and magnetic switching in thin films [27].

## II. THEORY

To motivate our measurement protocol, we first inspect the interferometric Ramsey method, which has been a standard method for early quantum sensing of waveforms [20]. In a Ramsey experiment, a superposition state, prepared by a first  $\pi/2$  pulse, evolves during a sensing time  $t$  and acquires a phase factor  $\phi(t)$  that is proportional to the transition frequency  $\omega_0$  between the ground and excited states [see Fig. 1(b)].

\*jzopes@phys.ethz.ch

†degenc@ethz.ch

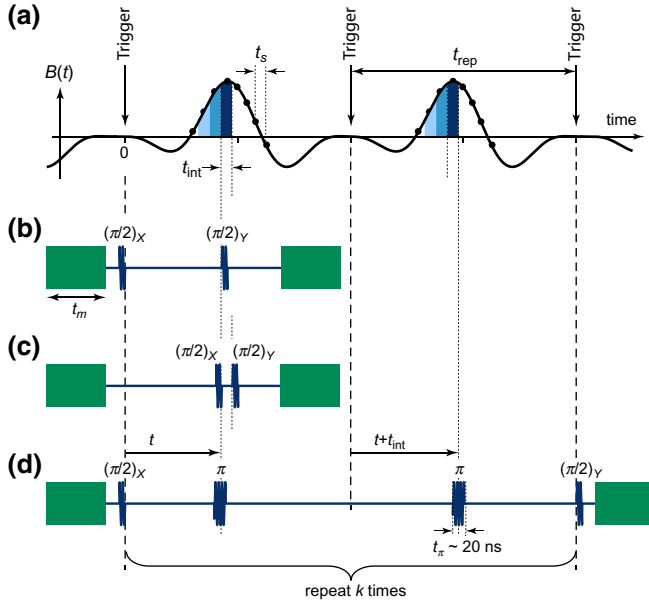


FIG. 1. Schemes for equivalent-time waveform sampling by a quantum sensor. (a) A schematic of a repetitive arbitrary waveform  $B(t)$ .  $t$  is the time relative to the preceding trigger and  $t_{\text{rep}}$  is the repetition time. The dots indicate the waveform sampling and  $t_s$  is the sampling time. (b) Standard integrative Ramsey detection of the waveform. The acquired sensor phase is proportional to the integral of the waveform between 0 and  $t$ . Signals are detected by stepping  $t$  in increments of  $t_s$ . Microwave pulses are shown in dark blue. The labels indicate the pulse angles and subscripts the pulse phases. Laser arm and readout pulses are shown in green. (c) Small-interval Ramsey detection of the waveform. (d) Differential echo detection of the waveform by spin echoes discussed in this work.  $t_{\text{int}}$  is the differential integration time and  $t_\pi$  is the  $\pi$ -pulse duration. The differential protocol can be repeated  $k$  times to linearly increase the accumulated phase.

For a spin sensor, where  $\omega_0$  is proportional to the component of the magnetic field along the spin's quantization axis, the acquired phase is as follows:

$$\phi(t) = \int_0^t \gamma_e B(t') dt'. \quad (1)$$

Here,  $B(t)$  is the time-dependent magnetic field that we aim to measure and  $\gamma_e$  is the gyromagnetic ratio of the spin. To extract the phase,  $\phi(t)$  is typically converted into a population difference  $p(t)$  by a second  $\pi/2$  pulse,

$$p(t) = \frac{1}{2} \{1 + \sin[\phi(t)]\} \stackrel{\phi \ll 1}{\approx} \frac{1}{2} [1 + \phi(t)], \quad (2)$$

followed by a projective readout of the sensor and signal averaging [2]. By measuring  $p(t)$  as a function of  $t$ , one thus effectively measures the integral of the magnetic field in the interval  $[0, t]$ . Using a numerical derivative, the magnetic field can subsequently be reconstructed [20].

However, this reconstruction greatly increases noise due to the derivative [28] and often requires phase unwrapping.

A more direct method that avoids numerical processing is the sampling of the waveform in small intervals,  $t_{\text{int}}$ , and building up the waveform by stepping  $t$ . The simplest approach is to use a Ramsey sequence with a very short integration time  $t_{\text{int}}$  [Fig. 1(c)]. In this case, the sensor phase  $\phi(t)$  encodes the field in the time interval  $[t, t + t_{\text{int}}]$ ,

$$\phi(t) = \int_t^{t+t_{\text{int}}} \gamma_e B(t') dt' \approx \gamma_e B(t) t_{\text{int}}, \quad (3)$$

without the need for numerical postprocessing. Due to the short  $t_{\text{int}}$ , one can often take advantage of the linear approximation ( $\sin \phi \approx \phi$ ) in Eq. (2). The short  $t_{\text{int}}$ , however, impairs sensitivity because  $\phi \propto t_{\text{int}}$ .

To maintain adequate sensitivity even for short  $t_{\text{int}}$ , we introduce a detection protocol that accumulates phase from several consecutive waveform passages. Our scheme requires that the repetition time is short,  $t_{\text{rep}} \ll T_2$ , where  $T_2$  is the sensor's coherence time, which is often the case for fast-waveform signals. Our protocol is shown in Fig. 1(d): By inserting two  $\pi$  pulses at times  $t$  and  $t + t_{\text{int}}$  relative to two consecutive waveform triggers, we selectively acquire phase from the time interval  $[t, t + t_{\text{int}}]$  while canceling the remaining phase accumulation. A similar scheme of partial phase cancellation has been implemented with digital Walsh filters [22] and Haar functions [23] via a sequence of  $\pi$  rotations. The linear recombination of sensor outputs in such waveform sampling, however, is prone to the introduction of errors, especially for rapidly varying signals the detection of which requires many  $\pi$  pulses [21]. In our scheme, the  $\pi$  rotations effectively act as an *in situ* derivative to the phase integral [Eq. (1)], bypassing the need for a later numerical differentiation or reconstruction. To further amplify the signal, the basic two- $\pi$ -pulse block can be repeated  $k$  times to accumulate phase from  $2k$  waveform passages, up to a limit set by  $2kt_{\text{rep}} \lesssim T_2$ . The amplified signal is (in a linear approximation)

$$p(t) = 0.5 + 2k\gamma_e B(t)t_{\text{int}}, \quad (4)$$

and when converted to magnetic field units,

$$B(t) = \frac{p(t) - 0.5}{2k\gamma_e t_{\text{int}}}. \quad (5)$$

### III. EXPERIMENTAL METHODS

We experimentally demonstrate arbitrary waveform sampling using the electronic spin of a single nitrogen-vacancy (N-V) center in a diamond single crystal. The N-V spin is initialized and read out using approximately 2- $\mu$ s-long green-laser pulses and a single-photon-counting

module [6]. Microwave control pulses are generated by an arbitrary waveform generator (AWG), amplified to reach Rabi frequencies of approximately 25 MHz and applied to the N-V center via a coplanar waveguide (CPW) structure [7]. Magnetic test waveforms are generated by a second function generator operated in burst mode and triggered by the AWG. The test signals are delivered to the N-V center either by injecting them into the common CPW using a bias-T [29] or by an auxiliary nearby microcoil [19,30]. The setup is operated in a magnetic bias field of 43 mT (aligned with the N-V crystal direction) to isolate the  $\{m_s = 0, m_s = -1\}$  manifold of the  $S = 1$  N-V spin and to achieve preferential alignment of the intrinsic nitrogen nuclear spin (here, the spin 1/2 of the  $^{15}\text{N}$  isotope) [31]. The latter is not required for our scheme but helps in reducing microwave pulse errors.

#### IV. RESULTS

We begin our study by recording a simple, 270-ns-long square waveform (Fig. 2). We record the waveform using both the standard integrative Ramsey scheme [Fig. 1(b)] and our differential-sampling technique [Fig. 1(d)]. For the Ramsey scheme, we reconstruct the magnetic waveform by a numerical differentiation of the raw signal [black data in Fig. 2(a)] via the central difference quotient of the smoothed signal [32]. The reconstructed waveform is shown in blue. For our differential-detection scheme, we directly plot the signal output without any further data processing [Fig. 2(b)]. Clearly, the differential-sampling method is able to faithfully reproduce the square pulse and is not affected by the noise amplification of the Ramsey scheme.

##### A. Time resolution

To characterize the time resolution of the method, we record the rising edge of the pulse with fine sampling  $t_s = 4$  ns [Fig. 2(c)]. We find a 10–90% step response time of  $\tau \sim 20$  ns. As detailed in Appendix A, the response time is approximately given by the following:

$$\tau \approx \frac{2}{\pi} \sqrt{t_\pi^2 + \frac{\pi}{2} t_{\text{int}}^2}, \quad (6)$$

since the finite pulse duration and the integration time act as moving average filters. While  $t_{\text{int}}$  can be deliberately adjusted,  $t_\pi$  is determined by the Rabi frequency of the system and sets a hard limit to the response time.

In Fig. 2(d), we show the corresponding transfer function  $G(\omega)$  of the sensor, i.e., the Fourier transform of the unit impulse response obtained from the step response. In our experiments, where  $t_{\text{int}} = t_\pi$ , the unit impulse response of the sensor is approximately given by a Hann function with characteristic length  $2t_\pi$  (see Appendix A). The Bode

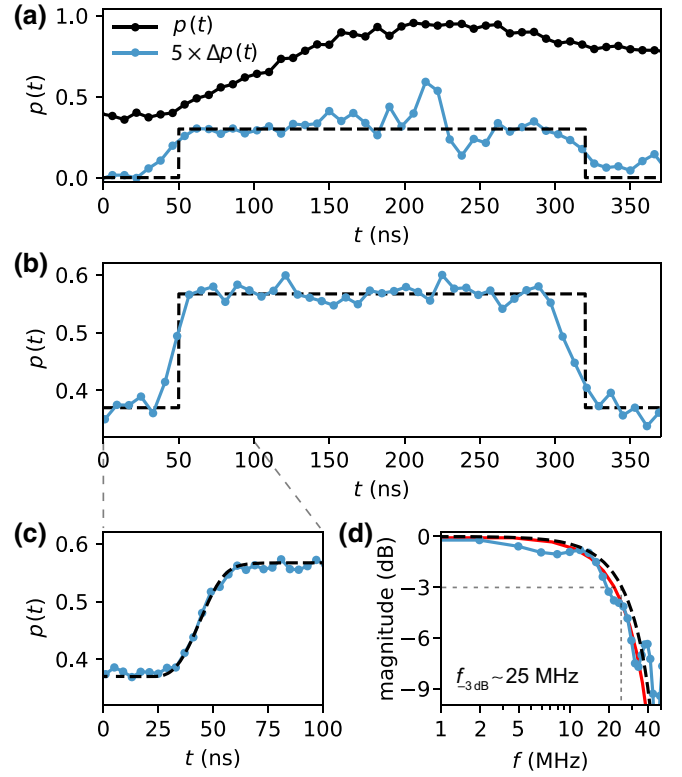


FIG. 2. Pulse detection and time resolution. (a) The sensor response to a square-wave magnetic signal (dashed curve) recorded using the standard integrative Ramsey method [protocol of Fig. 1(b)]. The raw data are shown in black and the reconstructed waveform is shown in blue. The waveform is reconstructed by applying a four-point moving average to the raw data and calculating the difference  $\Delta p$  between adjacent points. The dwell time is  $t_s = 8$  ns and the total averaging time is 1 h. (b) The sensor response (raw signal) to the same waveform signal recorded using the differential-spin-echo technique [protocol of Fig. 1(d)] using  $k = 2$ . The total averaging time is 15 min. The  $\pi$ -pulse and integration lengths are  $t_{\text{int}} = t_\pi = 20$  ns. (c) High-resolution sampling ( $t_s = 4$  ns) of the rising edge of the square-pulse waveform. The blue points are measured data. The dashed black line is the expected step response for  $\pi$ -pulse and integration lengths of  $t_{\text{int}} = t_\pi = 20$  ns. (d) The magnitude plot of the corresponding sensor transfer function. The blue dots are the data and the black dashed curve is the Fourier transform of a Hann window of duration  $2t_\pi = 40$  ns. The red curve additionally takes the finite response time of the test signal circuit (approximately 8 ns) into account.

plot indicates a  $-3$  dB sensor bandwidth  $f_{-3\text{dB}} \approx 25$  MHz, with good agreement between theory and experiments. According to Eq. (6), the fastest response time allowed by our Rabi frequency is  $\tau \sim 16$  ns (a bandwidth of approximately 40 MHz), obtained for  $t_{\text{int}} \rightarrow 0$ . Since the sensitivity scales with  $t_{\text{int}}$ , this limit cannot be reached in practice. The choice of  $t_{\text{int}} = t_\pi$  provides the fastest response before the sensitivity becomes unduly compromised.

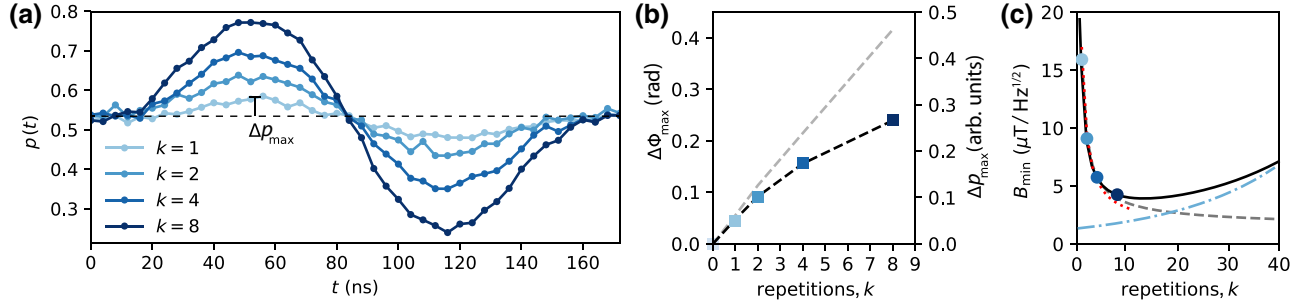


FIG. 3. Increased sensitivity by integrating  $2k$  waveform passages. (a) The sensor output  $p(t)$  for  $k = 1, 2, 4$ , and  $8$  repetitions of the two- $\pi$ -pulse unit [see Fig. 1(c)], for a sine waveform of amplitude  $10 \mu\text{T}$  and frequency  $f = 8 \text{ MHz}$ . The integration time and  $\pi$ -pulse duration are  $t_{\text{int}} = t_{\pi} = 20 \text{ ns}$  and the repetition time is  $t_{\text{rep}} = 344 \text{ ns}$ . (b) The peak output signal  $\Delta p_{\max}$  as a function of  $k$  (colored squares). The gray dashed line shows a linear scaling that would be expected in the absence of sensor decoherence. The black dash-dotted line takes decoherence into account ( $T_2 = 14 \mu\text{s}$ ). (c) The minimum detectable magnetic field  $B_{\min}$  per unit time as defined by Eq. (7) (black curve). The colored dots represent the data from (a). The dashed, dash-dotted, and dotted curves are explained in the text. The best experimental sensitivity is approximately  $4 \mu\text{T}/\sqrt{\text{Hz}}$  for  $k = 8$ .

### B. Enhanced sensitivity by repetitive phase accumulation

In a next step, we investigate the signal gain possible by accumulating phase from  $2k$  consecutive waveform passages. Figure 3(a) plots the sensor response from a weak sinusoidal test signal recorded with  $k = 1, 2, 4$ , and  $8$ . Clearly, a much larger oscilloscope response results for higher  $k$  values. To estimate the signal gain, we plot the peak sensor signal  $\Delta p_{\max}$  [indicated in (a)] as a function of  $k$  [see Fig. 3(b)]. At small  $k$  values, the increase of  $\Delta p_{\max}$  is proportional to  $k$ , as expected, while at larger  $k$ , decoherence of the sensor attenuates the signal. By correcting for sensor decoherence, we can recover the almost exact linear scaling of the signal phase  $\Delta\phi_{\max}$  with  $k$  [the dashed line in (b)].

To quantify the overall sensitivity in the presence of decoherence and sensor readout overhead, we calculate a minimum detectable field  $B_{\min}$ , defined as the input field that gives a unity signal-to-noise ratio for a 1-s integration time.  $B_{\min}$  for the differential-echo sequence is given by the following:

$$B_{\text{min,Diff}} = \frac{\sqrt{t_m + 2kt_{\text{rep}} \exp(2kt_{\text{rep}}/T_2)}}{\gamma_e C 2kt_{\text{int}}}, \quad (7)$$

where  $t_m = 3 \mu\text{s}$  is the arm and readout duration [see Fig. 1(b)],  $T_2 \sim 14 \mu\text{s}$  is the coherence time, and  $C \sim 0.02$  is a dimensionless number that quantifies the quantum-readout efficiency [2]. In Fig. 3(c), we plot  $B_{\min}$  as a function of  $k$ . We find that  $B_{\min} \propto k^{-1}$  for short durations  $kt_{\text{rep}} < t_m$ , that is, the benefit of repeating the sequence is largest for small  $k$  and high repetition rates (dotted curve). Once  $kt_{\text{rep}} > t_m$ , the scaling reduces to  $B_{\min} \propto k^{-0.5}$  because the linear phase accumulation now competes with standard signal averaging (dashed curve). For large values of  $kt_{\text{rep}}$  that exceed the sensor coherence time  $T_2$ , the

efficiency of the method rapidly deteriorates (dash-dotted curve). The optimum  $k$  is approximately  $k \approx T_2/(4t_{\text{rep}})$ .

The sensitivity of our differential-echo method [Eq. (7)] can be compared to that of the Walsh, Haar and the Ramsey methods [Eqs. (B3) and (B4), Appendix B]. We find that for short waveform durations  $t_{\text{rep}}$ , our method provides superior sensitivity compared to the Walsh and Haar scheme, due to the large repetition factor  $k$  (see Fig. 5). For long waveforms with low  $k$  and large  $N$ , the Walsh and Haar schemes tend to outperform our method due to their multiplexing advantage. In both regimes, the differential-echo and Walsh and Haar schemes provide a much higher sensitivity compared to the Ramsey scheme.

### C. Detection of a complex waveform

We complete our study by demonstrating the detection of a complex test waveform (Fig. 4). The waveform contains the sum of several Fourier components with the analytical expression for  $B(t)$  given in the figure caption. In Fig. 4(a), we show the experimentally measured waveform (light blue points) together with the input waveform (dashed black line) in the same plot. The experimental waveform consists of  $N = 280$  data points sampled at a  $t_s = 4 \text{ ns}$  horizontal resolution. Clearly, the experimental waveform agrees very well with the applied input. The experimental data are plotted without any data processing, demonstrating that our differential-sampling method directly reproduces the waveform signal. Figure 4(b) further presents the corresponding power spectra of the input waveform (black dashed line) and the recorded sensor output (light blue points). Although the signal lies within the analog bandwidth of the sensor (approximately  $25 \text{ MHz}$ ), some attenuation is observed at higher frequencies. If desired, inverse-filtering techniques could be



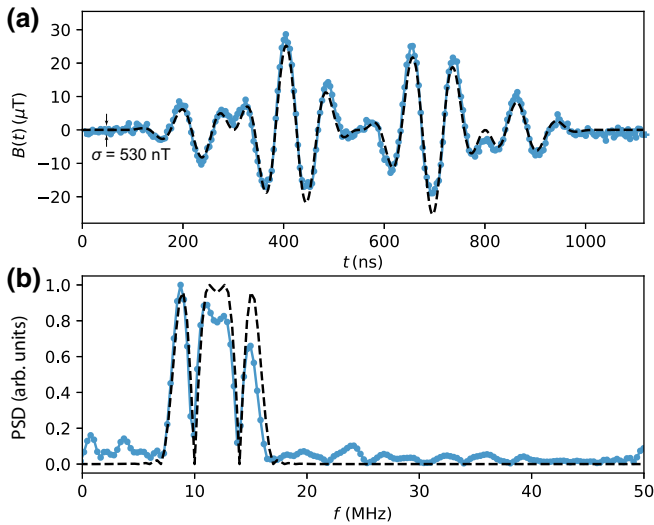


FIG. 4. An example of arbitrary waveform detection. (a) The input waveform (dashed line) and the recorded waveform data (blue dots) for a complex waveform given by  $B(t) = B \sin^2(\omega t/2) [\sin(12\omega t) \cos(\omega t) \sin^2(\omega t)]$ , with  $B = 81.87 \mu\text{T}$  and  $\omega = 2\pi \times 1 \text{ MHz}$ . The waveform is sampled using  $N = 280$  data points and  $t_s = 4 \text{ ns}$ . Further parameters are  $t_{\text{int}} = t_\pi = 20 \text{ ns}$ ,  $t_{\text{rep}} = 1400 \text{ ns}$ , and  $k = 4$ . The total experimental time is 60 h, corresponding to approximately  $1.44 \times 10^{10}$  waveform triggers. The baseline noise is  $\sigma \approx 530 \text{ nT rms}$ . (b) The normalized power spectra of the input waveform (black dashed line) and the detected waveform (light blue connected points). Fourier components at higher frequencies are slightly attenuated due to the limited bandwidth of the sensing sequence.

applied to compensate the high-frequency roll-off of the sensor.

Before concluding, we point out a few limitations and possible remedies of the differential-waveform sampling technique. First, our scheme is only applicable to waveforms that can be triggered twice within the sensor's  $T_2$  time. To extend  $T_2$  and allow for long repetition times, dynamical decoupling pulses could be added during the phase accumulation time of our protocol. As long as these pulses are identical during each waveform passage, they do not interfere with the differential-echo formation. While the effectiveness of dynamical decoupling depends on the specific experimental situation,  $T_2$  improvements of 2–3 orders of magnitude have been demonstrated in several qubit systems [33–35]. Second, the maximum peak-to-peak signal amplitude is limited by the excitation bandwidth of  $\pi$  pulses to  $(\gamma_e t_\pi)^{-1}$ , here approximately 2 mT. Only relatively weak fields can therefore be detected with our method. To cover strong signals, time-resolved spectroscopy techniques are available [19]. Third, when accumulating signal over many passages  $k$ , the phase may exceed the sensor's linear range [see Eq. (1)]. In this situation, the relative phase of the second  $\pi/2$  pulse could be cycled [36] to recover a linear response.

## V. OUTLOOK

In summary, we experimentally demonstrate a quantum sensing technique for direct detection of arbitrary waveforms in the time domain using equivalent time sampling. Our method does not require waveform reconstruction, allowing, for example, for the sampling of arbitrary segments from a longer waveform. Using a diamond N-V center as the sensor, we demonstrate a Rabi-frequency-limited time resolution of approximately 20 ns and a competitive magnetic sensitivity of approximately  $4 \mu\text{T}/\sqrt{\text{Hz}}$  for waveforms in the megahertz range.

Looking ahead, our scheme will be useful for investigating the spatiotemporal dynamics of photocurrent generation [26] or magnetic polarization switching [27]. In the experiment by Zhou and coworkers [26], the decay of photocurrent and interplay with temperature gradients in response to a local laser stimulus was investigated. Here, our scheme will allow the resolution of dynamics with much higher sensitivity and time resolution. The study of Baumgartner *et al.* [27] investigated the current-induced switching of Pt/Co/ $\text{AlO}_x$  magnetic dots, which hold promise for nonvolatile memory and logic units. Here, our technique provides an alternative to x-ray spectroscopy in synchrotron facilities. Since diamond magnetometry is also applicable to antiferromagnets [37–39], a broad range of magnetic switching and domain-wall propagation dynamics can potentially be studied. Although these dynamics are typically fast (approximately nanoseconds for ferromagnets), below the response time of our current experiment (approximately 20 ns), our scheme could still time tag the fast rising edge of the switching. The time resolution will be further improved by the use of miniaturized coplanar waveguides, which have been shown to support Rabi frequencies of 200 – 500 MHz for N-V centers [40,41], corresponding to  $\tau \sim 1 - 2.5 \text{ ns}$ .

## ACKNOWLEDGMENTS

We thank Pol Welter, Martin Wörnle, and Konstantin Herb for helpful discussions. This work has been supported by the Swiss National Science Foundation (SNFS), under Project Grant No. 200020\_175600, the National Center of Competence in Research in Quantum Science and Technology (NCCR QSIT), and the Advancing Science and TEchnology thRough dIamond Quantum Sensing (ASTERQIS) program of the European Commission, under Grant No. 820394.

## APPENDIX A: TRANSFER FUNCTION AND RESPONSE TIME

We derive the expression for the rise time  $\tau$  [Eq. (6) in the main text] and the transfer function shown by a dashed line in Fig. 2(d). According to Eq. (2) of the main text,

the probability function  $p$  of the sensor in the small-signal limit  $\phi \ll 1$  is given as follows:

$$p \approx \frac{1}{2}(1 + \phi).$$

The total phase accumulated over one cycle of the differential-echo sequence is given by the following:

$$\phi(t) = \int_0^{2t_{\text{rep}}} \gamma_e B(t') M(t, t') dt', \quad (\text{A1})$$

where  $t_{\text{rep}}$  is the repetition time of the waveform and  $M(t, t')$  is the modulation function [2] of the sensing sequence, defined below. Because the waveform function is repetitive,  $B(t' + t_{\text{rep}}) = B(t')$ , we can rewrite Eq. (A1) as follows:

$$\phi(t) = \int_0^{t_{\text{rep}}} \gamma_e B(t') [M_1(t, t') + M_2(t, t')] dt', \quad (\text{A2})$$

where  $M_1(t, t')$  and  $M_2(t, t')$  are the modulation functions of the two differential-spin-echo segments, both of which have a duration of  $t_{\text{rep}}$ . In the case of ideal short  $\pi$  pulses, the modulation functions are given by step functions:

$$M_1(t, t') = \begin{cases} +1 & : t' \leq t, \\ -1 & : t' > t; \end{cases} \quad (\text{A3})$$

$$M_2(t, t') = \begin{cases} -1 & : t' \leq t + t_{\text{int}}, \\ +1 & : t' > t + t_{\text{int}}. \end{cases} \quad (\text{A4})$$

In the case of finite pulse durations, the modulation functions are no longer abrupt step functions but, rather, are described by the Rabi nutation formula, where the value of  $M$  is proportional to the  $z$  projection of the qubit. For square  $\pi$  pulses of duration  $t_\pi$ , the modulation functions are given by the following:

$$M_1(t') = \begin{cases} -1 & : t' \leq t - t_\pi/2, \\ +\sin\left(\frac{[t' - t]}{t_\pi/\pi}\right) & : t - t_\pi/2 < t' \leq t + t_\pi/2, \\ +1 & : t' > t + t_\pi/2; \end{cases} \quad (\text{A5})$$

$$M_2(t') = \begin{cases} 1 & : t' \leq t + t_{\text{int}} - \frac{t_\pi}{2}, \\ -\sin\left(\frac{[t' - t - t_{\text{int}}]}{t_\pi/\pi}\right) & : t + t_{\text{int}} - \frac{t_\pi}{2} < t' \leq t + t_{\text{int}} + \frac{t_\pi}{2}, \\ -1 & : t' > t + t_{\text{int}} + \frac{t_\pi}{2}. \end{cases} \quad (\text{A6})$$

For the general case where  $t_{\text{int}} \neq t_\pi$ , we estimate the response time  $\tau$  through a set of numerical simulations of Eqs. (A1)–(A6). We compute the acquired sensor phase for varying  $t_{\text{int}}$  and  $t_\pi$  for a ideal step-input waveform and determine the response time of the sensor output for each pair  $(t_\pi, t_{\text{int}})$ . We find that the response time approximately

follows Eq. (6) in the main text:

$$\tau \approx \frac{2}{\pi} \sqrt{t_\pi^2 + \frac{\pi}{2} t_{\text{int}}^2}.$$

For the case where  $t_{\text{int}} = t_\pi$ , the transfer function can be computed analytically. The sum  $M \equiv M_1(t, t') + M_2(t, t')$  of the two modulation functions is given by the following:

$$M(t, t') = \begin{cases} 1 + \cos\left(\frac{\pi[t' - t - t_\pi/2]}{t_\pi}\right) & : t - \frac{t_\pi}{2} < t' \leq t + \frac{3t_\pi}{2}, \\ 0 & : \text{otherwise.} \end{cases} \quad (\text{A7})$$

The function  $M(t, t')$  is equivalent to a Hann function of characteristic duration  $2t_\pi$  that is centered at  $t' = t + t_\pi/2$ . The transfer function of the sensing sequence is thus given by the Fourier transform of the Hann function.

## APPENDIX B: SENSITIVITY ANALYSIS

We analyze the sensitivity of the differential-echo sequence and compare it with the sensitivity of the Walsh method presented in Ref. [22] and the time-resolved Ramsey method described by Fig. 2(c). According to Ref. [23], the Haar wavelet-sensing method provides the same sensitivity as the Walsh method.

The reconstructed field  $B(t)$  at time  $t$  using  $N$  measured Walsh coefficients  $\hat{B}_m$  is given by Ref. [22]:

$$B(t) = \sum_{m=0}^{N-1} \hat{B}_m w_m(t/t_{\text{rep}}). \quad (\text{B1})$$

Here,  $w_m(t/t_{\text{rep}})$  is the  $m$ th Walsh function, which oscillates between  $\pm 1$  in the interval  $[0, t_{\text{rep}}]$ . The minimum resolvable Walsh coefficient per unit time is given by an expression analogous to Eq. (7):

$$\hat{B}_{\text{min}} = \frac{\sqrt{t_m + t_{\text{rep}}} \exp(t_{\text{rep}}/T_2)}{\gamma_e C t_{\text{rep}}}. \quad (\text{B2})$$

Consequently, the minimum resolvable field at time  $t$ , according to error propagation, is given by the following:

$$\begin{aligned} B_{\text{min,Walsh}} &= \sqrt{\sum_{m=0}^{N-1} \hat{B}_{\text{min}}^2} = \sqrt{N} \hat{B}_{\text{min}} \\ &= \frac{\sqrt{N} \sqrt{t_m + t_{\text{rep}}} \exp(t_{\text{rep}}/T_2)}{\gamma_e C t_{\text{rep}}}. \end{aligned} \quad (\text{B3})$$

This expression can be compared to the minimum resolvable field for the differential-echo method, Eq. (7):

$$B_{\text{min,Diff}} = \frac{\sqrt{t_m + 2kt_{\text{rep}}} \exp(2kt_{\text{rep}}/T_2)}{\gamma_e C 2kt_{\text{int}}}.$$

Finally, for the time-resolved Ramsey method [Fig. 1(c)], the minimum detectable field is given by the following:

$$B_{\text{min,Ramsey}} = \frac{\sqrt{t_m + t_{\text{rep}}} \exp(t_{\text{int}}/T_2^*)}{\gamma_e C t_{\text{int}}}. \quad (\text{B4})$$

Note that to build up the full  $N$ -point waveform, a total of  $N$  measurements are needed for all methods. For the differential-echo and Ramsey methods, the waveform is measured point by point in the time domain. For the Walsh method,  $N$  Walsh coefficients must be measured.

To get an idea of the relative sensitivities of the three methods, we compare the errors for waveform parameters set by  $N = t_{\text{rep}}/t_{\text{int}}$  and  $k = T_2/(4t_{\text{rep}})$  and disregard dephasing and decoherence. For the differential-echo method, we find:

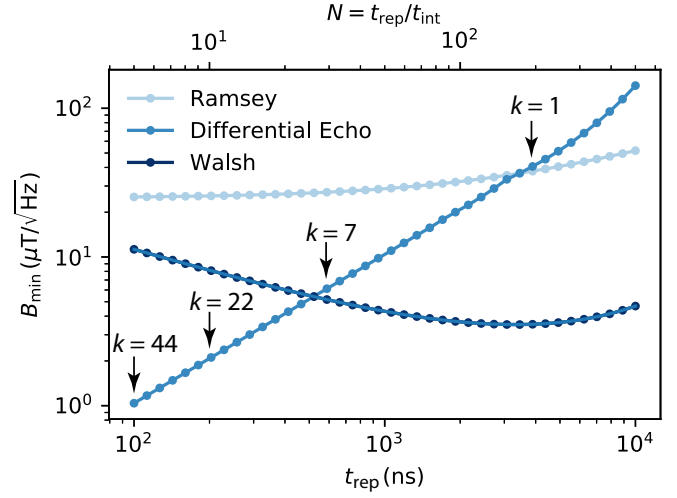


FIG. 5. The minimum detectable field per unit time for different waveform-sensing methods. We plot the minimum detectable field as a function of the waveform duration  $t_{\text{rep}}$ . We use parameters typical for our experiment,  $t_m = 3 \mu\text{s}$ ,  $T_2^* = 1.5 \mu\text{s}$ ,  $T_2 = 14 \mu\text{s}$ , and  $t_{\text{int}} = 20 \text{ ns}$ . For each  $t_{\text{rep}}$ , the number of waveform samples is set to  $N = t_{\text{rep}}/t_{\text{int}}$  and the repetition factor  $k$  of the differential-echo sequence is adjusted for optimum sensitivity according to Fig. 3(c).

$$B_{\text{min,Diff}} \approx \begin{cases} \frac{\sqrt{N}}{k} \left[ \frac{T_2}{t_m} \right]^{1/2} B_{\text{min,Walsh}} & \text{for } t_{\text{rep}} \ll t_m, \\ \sqrt{\frac{N}{k}} B_{\text{min,Walsh}} & \text{for } t_{\text{rep}} \gg t_m. \end{cases} \quad (\text{B5})$$

For the Ramsey method, we find the following:

$$B_{\text{min,Ramsey}} \approx \sqrt{N} B_{\text{min,Walsh}} \quad (\text{B6})$$

We find that the error of the differential-echo sequence is lowest for small  $N$  and large  $k$ , i.e., for short waveforms and long coherence times.

In Fig. 5, we plot the minimum detectable field per unit time as function of the duration of the waveform  $t_{\text{rep}}$  for the parameters used in our experiments. We find that for short waveforms ( $t_{\text{rep}} < 400 \text{ ns}$ , as in Figs. 2 and 3), the differential-echo technique provides the highest sensitivity. For longer waveforms ( $t_{\text{rep}} > 1 \mu\text{s}$ , as in Fig. 4), the Walsh method is superior in sensitivity. The sensitivity of the time-resolved Ramsey sequence is inferior to both sensing methods for the waveform durations considered in this work.

- [1] D. Budker and M. Romalis, Optical magnetometry, *Nat. Phys.* **3**, 227 (2007).
- [2] C. Degen, F. Reinhard, and P. Cappellaro, Quantum sensing, *Rev. Mod. Phys.* **89**, 035002 (2017).



- [3] G. Kucsko, P. C. Maurer, N. Y. Yao, M. Kubo, H. J. Noh, P. K. Lo, H. Park, and M. D. Lukin, Nanometre-scale thermometry in a living cell, *Nature* **500**, 54 (2013).
- [4] M. W. Doherty, N. B. Manson, P. Delaney, F. Jelezko, J. Wrachtrup, and L. C. Hollenberg, The nitrogen-vacancy colour centre in diamond, *Phys. Rep.* **528**, 1 (2013).
- [5] F. Dolde, H. Fedder, M. W. Doherty, T. Noebauer, F. Rempp, G. Balasubramanian, T. Wolf, F. Reinhard, L. C. L. Hollenberg, F. Jelezko, and J. Wrachtrup, Electric-field sensing using single diamond spins, *Nat. Phys.* **7**, 459 (2011).
- [6] M. Loretz, T. Rosskopf, and C. L. Degen, Radio-Frequency Magnetometry Using a Single Electron Spin, *Phys. Rev. Lett.* **110**, 017602 (2013).
- [7] J. Zopes, K. Sasaki, K. S. Cujia, J. M. Boss, K. Chang, T. F. Segawa, K. M. Itoh, and C. L. Degen, High-Resolution Quantum Sensing with Shaped Control Pulses, *Phys. Rev. Lett.* **119**, 260501 (2017).
- [8] G. de Lange, Z. Wang, D. Riste, V. Dobrovitski, and R. Hanson, Universal dynamical decoupling of a single solid-state spin from a spin bath, *Science* **330**, 60 (2010).
- [9] J. Bylander, S. Gustavsson, F. Yan, F. Yoshihara, K. Harrabi, G. Fitch, D. G. Cory, Y. Nakamura, J. S. Tsai, and W. D. Oliver, Noise spectroscopy through dynamical decoupling with a superconducting flux qubit, *Nat. Phys.* **7**, 565 (2011).
- [10] S. Schmitt, T. Gefen, F. M. Sturmer, T. Unden, G. Wolff, C. Muller, J. Scheuer, B. Naydenov, M. Markham, S. Pez-zagna, J. Meijer, I. Schwarz, M. Plenio, A. Retzker, L. P. McGuinness, and F. Jelezko, Submillihertz magnetic spectroscopy performed with a nanoscale quantum sensor, *Science* **356**, 832 (2017).
- [11] J. M. Boss, K. S. Cujia, J. Zopes, and C. L. Degen, Quantum sensing with arbitrary frequency resolution, *Science* **356**, 837 (2017).
- [12] S. Kotler, N. Akerman, Y. Glickman, A. Keselman, and R. Ozeri, Single-ion quantum lock-in amplifier, *Nature* **473**, 61 (2011).
- [13] R. S. Schoenfeld and W. Harneit, Real Time Magnetic Field Sensing and Imaging Using a Single Spin in Diamond, *Phys. Rev. Lett.* **106**, 030802 (2011).
- [14] N. De Zanche, C. Barmet, J. A. Nordmeyer-Massner, and K. P. Pruessmann, NMR probes for measuring magnetic fields and field dynamics in MR systems, *Magn. Reson. Med.* **60**, 176 (2008).
- [15] C. S. Shin, C. E. Avalos, M. C. Butler, D. R. Trease, S. J. Seltzer, J. P. Mustonen, D. J. Kennedy, V. M. Acosta, D. Budker, A. Pines, and V. S. Bajaj, Room-temperature operation of a radiofrequency diamond magnetometer near the shot-noise limit, *J. Appl. Phys.* **112**, 124519 (2012).
- [16] K. Jensen, R. Budvytyte, R. A. Thomas, T. Wang, A. M. Fuchs, M. V. Balabas, G. Vasilakis, L. D. Mosgaard, H. C. Starkind, J. H. Muller, T. Heimburg, S. Olesen, and E. S. Polzik, Non-invasive detection of animal nerve impulses with an atomic magnetometer operating near quantum limited sensitivity, *Sci. Rep.* **6**, 29638 (2016).
- [17] J. F. Barry, M. J. Turner, J. M. Schloss, D. R. Glenn, Y. Song, M. D. Lukin, H. Park, and R. L. Walsworth, Optical magnetic detection of single-neuron action potentials using quantum defects in diamond, *Proc. Natl. Acad. Sci. USA* **113**, 14133 (2016).
- [18] H. Xia, A. Ben-Amar Baranga, D. Hoffman, and M. V. Romalis, Magnetoencephalography with an atomic magnetometer, *Appl. Phys. Lett.* **89**, 211104 (2006).
- [19] J. Zopes, K. Herb, K. S. Cujia, and C. L. Degen, Three-Dimensional Nuclear Spin Positioning Using Coherent Radio-Frequency Control, *Phys. Rev. Lett.* **121**, 170801 (2018).
- [20] G. Balasubramanian, P. Neumann, D. Twitchen, M. Markham, R. Kolesov, N. Mizuochi, J. Isoya, J. Achard, J. Beck, J. Tissler, V. Jacques, P. R. Hemmer, F. Jelezko, and J. Wrachtrup, Ultralong spin coherence time in isotopically engineered diamond, *Nat. Mater.* **8**, 383 (2009).
- [21] E. Magesan, A. Cooper, H. Yum, and P. Cappellaro, Reconstructing the profile of time-varying magnetic fields with quantum sensors, *Phys. Rev. A* **88**, 032107 (2013).
- [22] A. Cooper, E. Magesan, H. N. Yum, and P. Cappellaro, Time-resolved magnetic sensing with electronic spins in diamond, *Nat. Commun.* **5**, 3141 (2014).
- [23] N. Xu, F. Jiang, Y. Tian, J. Ye, F. Shi, H. Lv, Y. Wang, J. Wrachtrup, and J. Du, Wavelet-based fast time-resolved magnetic sensing with electronic spins in diamond, *Phys. Rev. B* **93**, 161117 (2016).
- [24] K. Sasaki, K. M. Itoh, and E. Abe, Determination of the position of a single nuclear spin from free nuclear precessions detected by a solid-state quantum sensor, *Phys. Rev. B* **98**, 121405 (2018).
- [25] A. Nowodzinski, M. Chipaux, L. Toraille, V. Jacques, J. F. Roch, and T. Debuisschert, Nitrogen-vacancy centers in diamond for current imaging at the redistributive layer level of integrated circuits, *Microelectron. Reliab.* **55**, 1549 (2015).
- [26] B. B. Zhou, P. C. Jerger, K. Lee, M. Fukami, F. Mujid, J. Park, and D. D. Awschalom, Spatiotemporal mapping of photocurrent in a monolayer semiconductor using a diamond quantum sensor, arXiv:1903.09287 (2019).
- [27] M. Baumgartner, K. Garello, J. Mendil, C. O. Avci, E. Grimaldi, C. Murer, J. Feng, M. Gabureac, C. Stamm, Y. Acremann, S. Finizio, S. Wintz, J. Raabe, and P. Gambardella, Spatially and time-resolved magnetization dynamics driven by spin-orbit torques, *Nat. Nanotechnol.* **12**, 980 (2017).
- [28] Ian Knowles and Robert J. Renka, Methods for numerical differentiation of noisy data, *Electron. J. Differ. Eq.* **21**, 235 (2014).
- [29] T. Rosskopf, J. Zopes, J. M. Boss, and C. L. Degen, A quantum spectrum analyzer enhanced by a nuclear spin memory, *npj Quantum Inf.* **3**, 33 (2017).
- [30] J. Zopes, K. S. Cujia, K. Sasaki, J. M. Boss, K. M. Itoh, and C. L. Degen, Three-dimensional localization spectroscopy of individual nuclear spins with sub-angstrom resolution, *Nat. Commun.* **9**, 4678 (2018).
- [31] V. Jacques, P. Neumann, J. Beck, M. Markham, D. Twitchen, J. Meijer, F. Kaiser, G. Balasubramanian, F. Jelezko, and J. Wrachtrup, Dynamic Polarization of Single Nuclear Spins by Optical Pumping of Nitrogen-Vacancy Color Centers in Diamond at Room Temperature, *Phys. Rev. Lett.* **102**, 057403 (2009).
- [32] Charles Jordan, *Calculus of Finite Differences: Third Edition* (American Mathematical Society, New York, 2017).

- [33] C. A. Ryan, J. S. Hodges, and D. G. Cory, Robust Decoupling Techniques to Extend Quantum Coherence in Diamond, *Phys. Rev. Lett.* **105**, 200402 (2010).
- [34] S. Gustavsson, F. Yan, J. Bylander, F. Yoshihara, Y. Nakamura, T. P. Orlando, and W. D. Oliver, Dynamical Decoupling and Dephasing in Interacting Two-Level Systems, *Phys. Rev. Lett.* **109**, 010502 (2012).
- [35] H. S. Knowles, D. M. Kara, and M. Atature, Observing bulk diamond spin coherence in high-purity nanodiamonds, *Nat. Mater.* **13**, 21 (2013).
- [36] H. S. Knowles, D. M. Kara, and M. Atature, Demonstration of a Coherent Electronic Spin Cluster in Diamond, *Phys. Rev. Lett.* **117**, 100802 (2016).
- [37] I. Gross, W. Akhtar, V. Garcia, L. J. Martinez, S. Chouaieb, K. Garcia, C. Carretero, B. Arthelemy, P. Appel, P. Maletinsky, J. V. Kim, J. Y. Chauleau, N. Jaouen, M. Viret, M. Bibes, S. Fusil, and V. Jacques, Real-space imaging of non-collinear antiferromagnetic order with a single-spin magnetometer, *Nature* **549**, 252 (2017).
- [38] P. Appel, B. J. Shields, T. Kosub, N. Hedrich, R. Hubner, J. Fassbender, D. Makarov, and P. Maletinsky, Nanomagnetism of magnetoelectric granular thin-film antiferromagnets, *Nano Lett.* **19**, 1682 (2019).
- [39] M. Wörnle *et al.*, Private communication (2019).
- [40] G. D. Fuchs, V. V. Dobrovitski, D. M. Toyli, F. J. Heremans, and D. D. Awschalom, Gigahertz dynamics of a strongly driven single quantum spin, *Science* **326**, 1520 (2009).
- [41] F. Kong, P. Zhao, X. Ye, Z. Wang, Z. Qin, P. Yu, J. Su, F. Shi, and J. Du, Nanoscale zero-field electron spin resonance spectroscopy, *Nat. Commun.* **9**, 1563 (2018).